

Superresolution imaging method using phase-shifting digital lensless Fourier holography

Luis Granero¹, Vicente Micó^{2*}, Zeev Zalevsky³, and Javier García²

¹AIDO – Technological Institute of Optics, Color and Imaging, C/ Nicolás Copérnico 7, 46980, Paterna, Spain

²Departamento de Óptica, Univ. Valencia, C/Dr. Moliner, 50, 46100 Burjassot, Spain

³School of Engineering, Bar-Ilan University, Ramat-Gan, 52900 Israel

*Corresponding author: vicente.mico@uv.es

Abstract: A method which is useful for obtaining superresolved imaging in a digital lensless Fourier holographic configuration is presented. By placing a diffraction grating between the input object and the CCD recording device, additional high-order spatial-frequency content of the object spectrum is directed towards the CCD. Unlike other similar methods, the recovery of the different band pass images is performed by inserting a reference beam in on-axis mode and using phase-shifting method. This strategy provides advantages concerning the usage of the whole frequency plane as imaging plane. Thus, the method is no longer limited by the zero order term and the twin image. Finally, the whole process results in a synthetic aperture generation that expands up the system cutoff frequency and yields a superresolution effect. Experimental results validate our concepts for a resolution improvement factor of 3.

©2009 Optical Society of America

OCIS codes: (050.5080) Phase shift; (100.2000) Digital image processing; (070.0070) Fourier optics and signal processing; (090.1995) Digital holography; (100.6640) Superresolution.

References and links

1. A. Bachl and A. W. Lukosz, "Experiments on superresolution imaging of a reduced object field," *J. Opt. Soc. Am.* **57**, 163-169 (1967).
2. E. Abbe, "Beitrage zur theorie des mikroskops und der mikroskopischen wahrnehmung," *Archiv. Mikroskopische Anat.* **9**, 413-468 (1873).
3. W. Lukosz, "Optical systems with resolving powers exceeding the classical limit," *J. Opt. Soc. Am.* **56**, 1463-1472 (1966).
4. W. Lukosz, "Optical systems with resolving powers exceeding the classical limit II," *J. Opt. Soc. Am.* **57**, 932-941 (1967).
5. A. Shemer, D. Mendlovic, Z. Zalevsky, J. García and P. García-Martínez, "Superresolving Optical system with time multiplexing and computer decoding," *Appl. Opt.* **38**, 7245-7251 (1999).
6. A. I. Kartashev, "Optical systems with enhanced resolving power," *Optics Spectrosc.* **9**, 204-206 (1960).
7. J. D. Armitage, A. W. Lohmann, and D. P. Parish, "Superresolution image forming systems for objects with restricted lambda dependence," *Jpn. J. Appl. Phys.* **4**, 273-275 (1965).
8. M. A. Grim and A. W. Lohmann, "Superresolution image for 1-D objects," *J. Opt. Soc. Am.* **56**, 1151-1156 (1966).
9. H. Bartelt and A. W. Lohmann, "Optical processing of 1-D signals," *Opt. Commun.* **42**, 87-91 (1982).
10. A. W. Lohmann and D. P. Paris, "Superresolution for nonbirrefringent objects," *Appl. Opt.* **3**, 1037-1043 (1964).
11. A. Zlotnik, Z. Zalevsky, and E. Marom, "Superresolution with nonorthogonal polarization coding," *Appl. Opt.* **44**, 3705-3715 (2005).
12. Z. Zalevsky, P. García-Martínez, and J. García, "Superresolution using gray level coding," *Opt. Express* **14**, 5178-5182 (2006).
13. Z. Zalevsky, D. Mendlovic and A. W. Lohmann, "Superresolution optical system for objects with finite size," *Opt. Commun.* **163**, 79-85 (1999).
14. E. Sabo, Z. Zalevsky, D. Mendlovic, N. Konforti and I. Kiryushev, "Superresolution optical system using three fixed generalized gratings: experimental results," *J. Opt. Soc. Am. A* **18**, 514-520 (2001).

15. J. García, V. Micó, D. Cojoc, and Z. Zalevsky, "Full field of view super-resolution imaging based on two static gratings and white light illumination," *Appl. Opt.* **47**, 3080-3087 (2008).
16. Ch. J. Schwarz, Y. Kuznetsova and S. R. Brueck, "Imaging interferometric microscopy," *Opt. Lett.* **28**, 1424-1426 (2003).
17. V. Mico, Z. Zalevsky, and J. García, "Superresolution optical system by common-path interferometry," *Opt. Express* **14**, 5168-5177 (2006).
18. V. Mico, Z. Zalevsky, P. García-Martínez and J. García, "Synthetic aperture superresolution using multiple off-axis holograms," *J. Opt. Soc. Am. A* **23**, 3162-3170 (2006).
19. G. Indebetouw, Y. Tada, J. Rosen, and G. Brooker, "Scanning holographic microscopy with resolution exceeding the Rayleigh limit of the objective by superposition of off-axis holograms," *Appl. Opt.* **46**, 993-1000 (2007).
20. Y. Kuznetsova, A. Neumann, and S. R. J. Brueck "Imaging interferometric microscopy – approaching the linear system limits of optical resolution", *Opt. Express* **15**, 6651-6663 (2007).
21. V. Mico, Z. Zalevsky, and J. García, "Synthetic aperture microscopy using off-axis illumination and polarization coding," *Opt. Commun.* **276**, 209-217 (2007).
22. V. Mico, Z. Zalevsky, and J. García, "Common-path phase-shifting digital holographic microscopy: a way to quantitative imaging and superresolution," *Opt. Commun.* **281**, 4273-4281 (2008).
23. V. Mico, Z. Zalevsky, C. Ferreira, and J. García, "Superresolution digital holographic microscopy for three-dimensional samples," *Opt. Express* **16**, 19260-19270 (2008).
24. F. Le Clerc, M. Gross and L. Collot, "Synthetic aperture experiment in the visible with on-axis digital heterodyne holography," *Opt. Lett.* **26**, 1550-1552 (2001).
25. J. H. Massig, "Digital off-axis holography with a synthetic aperture", *Opt. Lett.* **27**, 2179-2181 (2002).
26. R. Binet, J. Colineau, and J-C. Leheureau, "Short-range synthetic aperture imaging at 633 nm by digital holography", *Appl. Opt.* **41**, 4775-4782 (2002).
27. J. Di, J. Zhao, H. Jiang, P. Zhang, Q. Fan, and W. Sun, "High resolution digital holographic microscopy with a wide field of view based on a synthetic aperture technique and use of linear CCD scanning," *Appl. Opt.* **47**, 5654-5658 (2008).
28. Ch. Liu, Z. Liu, F. Bo, Y. Wang, and J. Zhu, "Super-resolution digital holographic imaging method," *Appl. Phys. Lett.* **81**, 3143-3145 (2002).
29. C. Yuan, H. Zhai, and H. Liu, "Angular multiplexing in pulsed digital holography for aperture synthesis," *Opt. Lett.* **33**, 2356-2358 (2008).
30. M. Paturzo, F. Merola, S. Grilli, S. De Nicola, A. Finizio, and P. Ferraro, "Super-resolution in digital holography by two-dimensional dynamic phase grating," *Opt. Express* **16**, 17107-17118 (2008).
31. I. Yamaguchi and T. Zhong, "Phase-shifting digital holography," *Opt. Lett.* **22**, 1268-1270 (1997).
32. I. Yamaguchi, J. Kato, S. Ohta, and J. Mizuno, "Image formation in phase-shifting digital holography and applications to microscopy," *Appl. Opt.* **40**, 6177-6185 (2001).
33. J. Goodman, *Introduction to Fourier Optics* 2nd ed., (McGraw-Hill, New York, 1996).
34. T. Kreis, *Handbook of Holographic Interferometry*, (Wiley-VCH, 2005).

1. Introduction

More than 40 years ago, Bachl and Lukosz presented a superresolving optical system [1] capable to overcome the spatial resolution limit imposed by diffraction [2]. Such method took part from a wider collection of techniques where different superresolution strategies were defined as a function of the object classification using a priori information [3,4]. By stating that the number of degrees of freedom of an imaging system remains constant, Lukosz theorized that any parameter in the system could be extended above the classical limit if any other factor is proportionally reduced. In particular, the spatial bandwidth could be improved by "paying" in others domains in which the object is independent to a given degree of freedom (a priori knowledge). Thus, one can find angular multiplexing for non-extended objects [1,3], time multiplexing for temporally restricted objects [4,5], spectral encoding for wavelength restricted objects [6,7], spatial multiplexing with one-dimensional objects [3,8,9], polarization coding with polarization restricted objects [10,11], and gray level multiplexing for objects with restricted intensity dynamic range [12].

Coming back to the Bachl and Lukosz approach [1], the gain in spatial bandwidth is achieved by reducing the object field of view. Two static masks (typically gratings) are inserted into conjugate planes at the object and image space of the experimental setup. The

encoding mask (at the object space) allows the transmission of additional diffracted object waves through the limited system aperture in such a way that they will not be transmitted through it in absence of the mask. The role of the decoding mask (at the image space) is to redefine the propagation direction of the new diffracted components as they were generated in the input object. However, a necessary condition must be fulfilled: the object field needs to be limited around the object region of interest in order to avoid image distortion coming from the ghost images produced in the encoding-decoding process.

Some modifications of the Bachl and Lukosz basic setup that also consider static gratings had been proposed along the years [13-15]. In any case, a hand-waving explanation of the underlying principle of any superresolving approach starts as follows. For fixed illumination wavelength, the resolving power of an imaging system is limited by diffraction as a function of its numerical aperture (NA) [2]. Or in other words, the limited aperture of the imaging system defines a cutoff frequency over the object's spatial-frequency content. In addition, the aim of the superresolution techniques is to widen such limited aperture allowing the generation of a synthetic aperture which expands up such cutoff frequency limit. This synthetic enlargement in the aperture implies an improvement in the resolution limit without changes in the physical properties of the optical system in comparison with the spatial resolution presented by the same optical system without applying the superresolved approach.

Classically, one of the most appealed payments to allow superresolved imaging is done with the time domain [4,5]. Thus, the method for synthetic aperture generation is based on time multiplexing the spatial frequency content diffracted by the input object. Such approaches can be implemented using off-axis illumination in digital holographic microscopy [16-23] or by shifting the CCD in digital holography [24-27].

In the last years, the original idea proposed by Bachl and Lukosz in 1967 has been performed in combination with digital holography [28-30]. The basic idea consists on the recording of a multiplexed hologram composed by the addition of individual ones where each one contains information about different spatial frequency regions of the diffracted object spectrum. Since Fourier-lensless off-axis configuration is implemented in the holographic recording, each band pass image can be recovered by digital fast Fourier transformation of the multiplexed hologram since the hologram diffraction orders do not overlap. And finally a superresolved image is generated by properly managing the different recovered band pass images. However, off-axis holographic configuration suffers from the spatial separation of the different diffraction orders in the hologram's Fourier domain. This fact means that the whole frequency plane is not accessible under imaging purposes. Thus, strong field of view restrictions must be considered to allow separation in the Fourier plane of the different diffraction orders and band pass images.

In this paper, we present a combination of methods never used before allowing superresolution effect in digital lensless Fourier holography with improved capabilities regarding previous attempts [28-30]. As in previous methods [1,13-15,28,30], the use of a diffraction grating in the imaging arm of the interferometric configuration allows that additional spatial-frequency bands of the spectrum diffracted by the object will be redirected towards the CCD in such a way that, without the grating, they would fall outside the aperture defined by the CCD recording device. However, in the proposed method we consider on-axis reference beam reintroduction in the CCD plane and the use of phase-shifting method [31,32] to recover the different band pass images. Phase-shifting in on-axis recording permits the use of the whole frequency plane as imaging plane because uses both an on-line recording setup to increase the fringe spacing and phase-shifting of the reference beam to evaluate directly the complex amplitude at the CCD plane. Thus, the recovered band pass images are no longer limited by the presence of the zero diffraction order and its conjugate image and the space-bandwidth product of the imaging system becomes optimized. Due to that frequency plane optimization, we can choose between two different possibilities. On one hand, superresolved imaging can be obtained over a large object field of view. On the other hand, a high number of

band pass images can be taken into account to get the superresolution effect if we limit the object's field of view. In this contribution, we have experimentally achieved for the first time a resolution gain factor of 3 while maximizing the object field of view because only 3 diffraction orders are considered. Moreover, as consequence of inserting a grating in the setup, vignetting problems in the reconstructed image are avoided.

The paper is organized as follows. Section 2 provides both qualitative system description and mathematical background of the experiment. Section 3 presents experimental results showing the resolution improvement. Section 4 concludes the paper.

2. Analysis of the proposed method

2.1 System description

The optical assembly used to demonstrate the capabilities of the proposed approach is depicted in Fig. 1. It is basically a Mach-Zehnder interferometric architecture in which a laser beam (incoming from a He-Ne laser source) is used as illumination wavelength. Thus, the object under test is illuminated in transmission mode and a Fresnel diffracted pattern is recorded by the CCD imaging device. Let us first to consider that no other optical elements are placed between the input plane and the CCD. Such diffracted pattern is combined at the CCD with a reference beam incoming from a spatial filter by the action of a beam splitter cube. The reference beam is a spherical divergent beam having the particularity that the distance (z_0) between the object and the CCD is equal to the pinhole-CCD distance, configuring a lensless Fourier transform hologram setup [33].

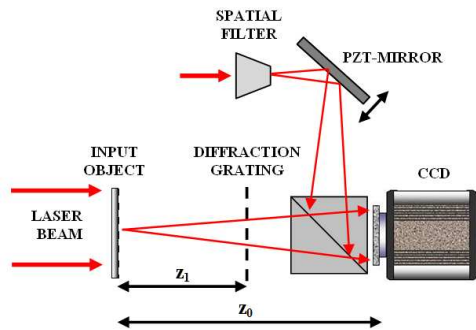


Fig. 1. Experimental setup used in the validation of the proposed approach.

Under this experimental assembly, the Fourier transform of the recorded interference pattern gives the in-focus on-axis band pass image of the object under test. Such image will have a resolution limit defined by either the NA of the imaging system or the geometrical resolution defined by the pixel size of the CCD detector. Since we are working with low NA values, from now on we assume that the NA which is being the limiting factor. Thus, the CCD full size and the distance between the object and the CCD will define the system NA and thus the cutoff frequency that limits the resolution of the system for a given wavelength. We refer to this configuration as conventional imaging mode along the manuscript.

However, it is possible to overcome the above established resolution limit by placing a diffraction grating between the object and the CCD [28,30]. Obviously, the diffraction grating must be properly selected (basic frequency and position). Figure 2 illustrate the operating principle for a 1D case. For sake of simplicity, we consider the axial point of the object. The diffracted spectrum has been divided into rectangular portions according with the CCD size (aperture of the conventional imaging system). Without the grating, only the central portion will reach the CCD area [case (a)]. With the grating, the zero order of the grating does not affect the propagation of the different spectral portions [case (b)] but the grating diffracts

additional spatial-frequency portions towards the CCD aperture [case (c)]. Since this new spectral portions reach obliquely the CCD, it will be possible to recover separately each one of them because they will not overlap at the Fourier domain. Once again, this separation depends on the properly selection of the diffraction grating.

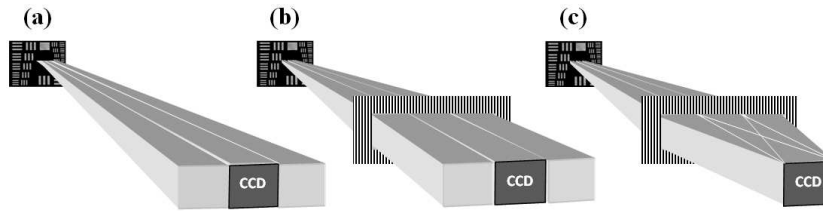


Fig. 2. Schematic figure representative of the proposed approach for a 1D case.

At this point, two methods can be used for recover the complex amplitude distribution of the different band pass images at the Fourier domain. The difference between them is the way that the reference beam is inserted at the CCD plane. On one hand, we can use off-axis holographic recording and windowed Fourier filtering. And on the other hand, we can use on-axis holographic configuration and phase-shift in one of the two interferometric beams (typically the reference beam). The former method needs only one interferogram to recover the band pass images but suffers from the presence of the zero order term and the set of twin images (one to each band pass image) at the Fourier domain. This fact means a high restriction over the accessible area of the frequency plane that is useful for imaging. The way to overcome this limitation is by considering the latter method. The phase-shift in the reference beam modulates those interferometric terms that are multiplied by the reference beam in such a way that it can be recovered separately after applying the phase-shifting algorithm. Since the phase-shifting method does not requires separation of the hologram orders at the Fourier domain, the whole frequency plane can be used for imaging. So, the space-bandwidth product of the system becomes optimized.

In this paper, we propose the use of an on-line configuration with phase-shifting approach to optimize the Fourier domain which is used as imaging space due to the lensless Fourier holographic configuration. Thus, the only restriction is due to the object field of view that can cause overlapping between the different recovered band pass images. Once again, we are in a similar case as in the Bach and Lukosz approach where the object field of view needs to be restricted in order to achieve superresolution effect. However, the restriction imposed by the proposed configuration is not as severe as in the case of the off-axis configuration. In order to control the non-overlapping between the object field of view in the recovered band pass images, we have included an adjustable square diaphragm attached to the input object.

In the phase-shifting procedure, we have applied a saw-tooth displacement in the piezo-mirror of the reference branch to allow continuous shift in the reference beam. Thus, it is simple to calculate the phase-shift cycle by correlation of one captured image with the remaining images that integrate the captured cycle. In our case, 60 subsequent images integrate the full phase-shifting cycle. After applying a conventional phase-shifting algorithm [34], all the band pass images are recovered in a single image and can be filtered separately in order to assemble the final superresolved image.

But in order to synthesize a high quality superresolved image, two factors must be taken into account. As first one, we find that the different diffracted bands will travel a different optical path before arriving at the CCD. This fact means that each band pass image will present a different global phase after the recovery process and must be compensated in the digital post-processing stage. And as second factor we find the correct repositioning of each recovered spectral band to its original position at the object spectrum. By knowing the distances in the system, the illumination wavelength and the grating period, it is possible to

add a linear phase factor to the different band pass images in order to shift the spectral content to a rough position in the spatial-frequency domain. A final fine adjustment is achieved by the addition of smaller linear phase factors in both horizontal and vertical directions. Also, this fine tuning process compensates phase variations incoming from misalignments in the optical setup. This procedure is repeated for every additional band pass image considered in the experiment and the full adjustment can be guided and automated by an image quality criterion.

2.2 Theoretical analysis

In this section we review the mathematical basis of the proposed approach. In our analysis we assume a 1D distribution in order to ease the mathematical treatment. However the expansion for the 2D case is straightforward. We denote by $t(x)$ the amplitude distribution of the input object. To take into account the effect of grating positioned at a given distance from the object, we propagate the field distribution of the input object to the grating location, multiply by the grating and then back propagate the light to the original input plane. Using this strategy, the input field distribution after free space propagation of z_I is proportional to

$$U(x_1) = \exp\left\{i\frac{k}{2z_1}x_1^2\right\} \int t(x) \exp\left\{i\frac{k}{2z_1}x^2\right\} \exp\left\{-i\frac{k}{2z_1}2x_1x\right\} dx \quad (1)$$

k being the wave number and x, x_I the spatial coordinates at the input plane and at a plane placed at z_I from the input plane, respectively. Eq. 1 is multiplied by the grating resulting in

$$U(x_1) = \exp\left\{i\frac{k}{2z_1}x_1^2\right\} \int t(x) \exp\left\{i\frac{k}{2z_1}x^2\right\} \exp\left\{-i\frac{k}{2z_1}2x_1x\right\} dx \sum_n B_n \exp\left\{-i2\pi\frac{n}{p}x_1\right\} \quad (2)$$

p, n and B_n being the period, the number of diffraction orders, and the coefficients of the different diffraction orders of the grating, respectively. The diffraction grating period will depend on the CCD lateral size, and on the object-CCD and the object-grating distances. The basic condition that must be fulfilled is that the central ray going to the first band pass will be deflected by the grating to the CCD center. Naming α_0 and α_I the angle of this ray to the optical axis and the angle after the grating deflection, respectively, the grating period must be

$$p = \frac{\lambda}{\sin \alpha_0 + \sin \alpha_I} \quad (3)$$

where the angles are given by

$$\tan \alpha_0 = \frac{\Delta x}{z_0} \quad \text{and} \quad \tan \alpha_I = \frac{z_1 \Delta x}{z_0(z_0 - z_1)} \quad (4)$$

For the case of paraxial approximation, the grating period has a simple expression

$$p = \frac{\lambda(z_0 - z_1)}{\Delta x} \quad (5)$$

where we can see as the period of the grating decreases as z_I increases from 0 to z_0 . Thus, when the grating is approaching to the CCD position ($z_I \sim z_0$), we need a small grating period (or high basic frequency) to fulfill our basic condition. And when the grating is placed near to

the object ($z_I \sim 0$), we need a large grating period (or low basic frequency). But the first case ($z_I \sim z_0$) will exhibit aliasing problems in the recorded hologram while the second one ($z_0 \sim 0$) will produce overlapping of the different band pass images at the Fourier domain. So, the condition defined by $z_0 \cong 2z_I$ is the most suitable from an experimental point of view.

Continuing with our propagation procedure, Eq. 2 is now back propagated ($-z_I$) to the input plane. The resulting input's amplitude distribution including the grating effect is

$$U(x) = C \sum_n B_n t\left(x - \frac{nz_1\lambda}{p}\right) \exp\left\{-i2\pi \frac{n}{p} x\right\} \quad (6)$$

where C is a constant that includes all the constant factors. Note that, if no grating is considered, the amplitude distribution provided by Eq. 6 coincides with that of the input object. Eq. 6 is now propagated in free space a distance of z_0 from the input plane to the CCD

$$U_I(x') = C' \sum_n \exp\left\{i \frac{k}{2z_0} x'^2\right\} \int t\left(x - \frac{nz_1\lambda}{p}\right) \exp\left\{i \frac{k}{2z_0} x^2\right\} \exp\left\{-i2\pi \left(\frac{x'}{\lambda z_0} - \frac{n}{p}\right) x\right\} dx \quad (7)$$

where C' is a constant. Eq. 7 is gives the amplitude distribution at the CCD plane through the imaging branch. Eq. 7 corresponds with the addition of several Fresnel transformations, each one corresponding with different shifted replicas of the input object function (first term inside the integral). Moreover, such replicas are shifted according to the period and position of the grating in the experimental setup. And those shifts are applied to $t(x)$, that is, to the amplitude distribution of the input object, prior to the propagation. This fact is equivalent to shifting the object at the input plane and it is the source of the vignetting problem in the experimental setup as we will detail in subsection 3.1.

The total amplitude distribution at the CCD plane comes from the addition of Eq. 7 and an on-axis spherical reference beam diverging from the same distance z_0 :

$$U_R(x', t) = R_0 \exp\left\{i \frac{k}{2z_0} x'^2\right\} \exp\{i\phi(t)\} \quad (8)$$

where R_0 is the amplitude of the reference beam, and $\phi(t)$ a linear phase variable in time and according to the phase-shifting procedure. Thus, the CCD records the output intensity distribution provided by the addition of Eqs. 7 and 8 and multiplied by the rectangular size of the CCD that trims the recording area at the output plane. For the sake of simplicity, let us assume that the grating has only 3 diffraction orders, that is: $n = -1, 0, +1$. In this case and leaving aside constant factors, Eq. 7 can be rewritten as

$$\begin{aligned} U_I(x') &= \exp\left\{i \frac{k}{2z_0} x'^2\right\} \int t\left(x + \frac{z_1\lambda}{p}\right) \exp\left\{i \frac{k}{2z_0} x^2\right\} \exp\left\{-i2\pi \left(\frac{x'}{\lambda z_0} + \frac{1}{p}\right) x\right\} dx \\ &+ \exp\left\{i \frac{k}{2z_0} x'^2\right\} \int t(x) \exp\left\{i \frac{k}{2z_0} x^2\right\} \exp\left\{-i2\pi \frac{x'}{\lambda z_0} x\right\} dx \\ &+ \exp\left\{i \frac{k}{2z_0} x'^2\right\} \int t\left(x - \frac{z_1\lambda}{p}\right) \exp\left\{i \frac{k}{2z_0} x^2\right\} \exp\left\{-i2\pi \left(\frac{x'}{\lambda z_0} - \frac{1}{p}\right) x\right\} dx \\ &= O_{-1}(x') + O_0(x') + O_{+1}(x') = \sum_{n=-1}^1 O_n(x') \end{aligned} \quad (9)$$

where $O_n(x')$ represents the different arriving bands at the CCD as consequence of the grating diffraction orders. Hence, the intensity distribution provided by the CCD at a given instant is

$$\begin{aligned}
I_{CCD}(x') &= \left| O_{-1}(x') + O_0(x') + O_{+1}(x') + U_R(x') \right|^2 \\
&= |O_{-1}(x')|^2 + |O_0(x')|^2 + |O_{+1}(x')|^2 + |U_R(x')|^2 \\
&\quad + O_{-1}(x')O_0^*(x') + O_0(x')O_{-1}^*(x') + O_0(x')O_{+1}^*(x') + O_{+1}(x')O_0^*(x') \\
&\quad + O_{-1}(x')O_{+1}^*(x') + O_{+1}(x')O_{-1}^*(x') \\
&\quad + [O_{-1}(x') + O_0(x') + O_{+1}(x')]U_R^*(x') \\
&\quad + [O_{-1}^*(x') + O_0^*(x') + O_{+1}^*(x')]U_R(x')
\end{aligned} \tag{10}$$

and the following analysis can be performed in Eq. 10. The second line contains the autocorrelation of the different interferometric terms that it will be centered at the Fourier domain. The third line is the cross-correlation between the zero order term and the additional bands provided by the grating. These 4 terms will be shifted from the origin at the Fourier domain according with the angle between them. The fourth line is similar to the previous one but it defines a higher angle in the recording process since it involves the cross-correlation of the diffracted bands provided by the grating. We can conceptually include all those terms into the zero order of the recorded hologram since they are not depending on the reference beam. And finally, the last two lines are related with the cross terms between the reference and imaging beams. Or in other words, the real (fifth line) and the twin (sixth line) images of the recorded hologram. Since the phase-shift is performed in the reference beam, the reference beam modulates the real and twin images and, after applying the whole process, either the real or the twin image can be recovered without the zero order term and without twin or real image, respectively. To our convenience, let us rewrite Eq. 10 as

$$\begin{aligned}
I_{CCD}(x',t) &= \left| \sum_{n=-1}^1 O_n(x') + U_R(x') \right|^2 \\
&= \sum_{n=-1}^1 |O_n(x')|^2 + \sum_{\substack{n,m=-1 \\ n \neq m}}^1 O_n(x')O_m^*(x') + \sum_{n=-1}^1 O_n(x')U_R^*(x') + \sum_{n=-1}^1 O_n^*(x')U_R(x') \\
&= \sum_{n=-1}^1 |O_n(x')|^2 + \sum_{\substack{n,m=-1 \\ n \neq m}}^1 O_n(x')O_m^*(x') \\
&\quad + \sum_{n=-1}^1 O_n(x')R_0 \exp\left\{-i\frac{k}{2z_0}x'^2\right\} \exp\{-i\phi(t)\} \exp\{-i\phi_n(x')\} \\
&\quad + \sum_{n=-1}^1 O_n^*(x')R_0 \exp\left\{i\frac{k}{2z_0}x'^2\right\} \exp\{i\phi(t)\} \exp\{i\phi_n(x')\}
\end{aligned} \tag{11}$$

$\phi_n(x')$ being the initial phase difference between imaging and reference beams which is directly related with the transmitted phase distribution of the different object bands. Assuming that the time dependence of the different recorded intensities is a function of the intensity image number p multiplied by the phase step between two consecutive images ($\phi(t)=p\phi_K$), Eq. 11 can be rewritten as follows when capturing the different intensity images in time sequence

$$I_{CCD}(x',t) = \sum_{n=-1}^1 |O_n(x')|^2 + \sum_{\substack{n,m=-1 \\ n \neq m}}^1 O_n(x') O_m^*(x') + R_0^2 \\ + 2R_0 \operatorname{Re} \left[\sum_{n=-1}^1 O_n(x') \exp \left\{ -i \frac{k}{2z_0} x'^2 \right\} \right] \cos(p\phi_k + \phi_n(x')) \quad (12)$$

Now, the phase-shift algorithm computes the different intensity distributions stored in time sequence by the CCD and recovers the phase distribution of the different frequency bands of the object [22,34]. In particular, we have applied a method that involve $m=60$ intensity images in one phase-shift period and permits the recovering of the summation of the initial phase distribution according to

$$\sum_{n=-1}^{+1} \phi_n(x') = \arctan \frac{-\sum_{i=1}^m I_i(x') \sin \left[\frac{2\pi}{m}(i-1) \right]}{\sum_{i=1}^m I_i(x') \cos \left[\frac{2\pi}{m}(i-1) \right]} \quad (13)$$

Once the phase-shifting method is applied, the recovered real image term (fifth line in Eq. 10) can be rewritten as

$$I_{CCD}(x') = [O_{-1}(x') + O_0(x') + O_{+1}(x')] U_R^*(x') \\ = \left[C'' \sum_{n=-1}^1 \int t \left(x - \frac{nz_1 \lambda}{p} \right) \exp \left\{ i \frac{k}{2z_0} x^2 \right\} \exp \left\{ -i2\pi \left(\frac{x'}{\lambda z_0} - \frac{n}{p} \right) x \right\} dx \right] \operatorname{rect} \left(\frac{x'}{\Delta x} \right) \quad (14) \\ = \left[C'' \sum_{n=-1}^1 FT \left\{ t \left(x - \frac{nz_1 \lambda}{p} \right) \right\}_u \otimes FT \left\{ \exp \left\{ i \frac{k}{2z_0} x^2 \right\} \right\}_u \right] \operatorname{rect} \left(\frac{x'}{\Delta x} \right)$$

C'' being the new redefined constant, $u = \frac{x'}{\lambda z_0} - \frac{n}{p}$ the scale factor of the Fourier transformation and the *rect* function represents the CCD limited size having a width of $\Delta x = 2z_0 NA$ in the x direction (NA being the numerical aperture of the experimental configuration). Notice that the action of the reference beam is, aside the temporal modulation performed by the phase-shifting process, to cancel the quadratic phase factor outside the integral in Eq. 7 in such a way that the image of the input object is now achievable by the Fourier transformation of Eq. 14. The recovered distribution after applying the proposed approach is related with different band-pass images of the input object selected by the position and the period of the grating that are multiplied by a quadratic phase factor related with the axial point of the input plane and representative of the imaging beam divergence after being convolved with the Fourier transformation of the CCD rectangular area

$$FT \{ I_{CCD}(x') \} = \left[D \exp \left\{ i \frac{k}{2d} u^2 \right\} \sum_{n=-1}^1 t \left(u + \frac{nz_1}{pz_0} \right) \exp \{ -i2\pi au \} \right] \otimes FT \left\{ \operatorname{rect} \left(\frac{x'}{\Delta x} \right) \right\} \quad (15)$$

where D is the new global constant, d is related with the propagation distance z_0 ($d = 1/\lambda^2 z_0$), and a is defined from the propagation distance and the basic period of the grating ($a = 2\lambda n z_0 / p$).

Conceptually talking, we can extract two conclusions from Eq. 15. From an object field point of view, the object shift at the input plane means a vignetting problem avoidance since the extra-axial points of the object are redirected towards the CCD. Thus, the intensity at the borders of the final reconstructed image will not be distorted. And from a spatial-frequency point of view, the linear exponential means that each shifted image will contain a different spectral range. So a final image having a wider spatial-frequency content could be synthesized in a later stage.

3. Experimental implementation

In this section we present experimental validation of the proposed approach considering two subsections. The first one is aimed to provide a deeper understanding of the approach by simply presenting the method step by step while showing a 1D resolution improvement. And the second one demonstrates a 2D superresolved image incoming from the use of the whole frequency plane as imaging plane. In both cases, we used a He-Ne laser (632nm emitting wavelength) as illumination source, a CCD (Basler A312f, 582x782 pixels, 8.3 μm pixel size, 12 bits/pixel) as imaging device, and a 25 μm pinhole as spherical divergent reference beam.

3.1 Superresolution imaging for a 1D test object case

To show how the proposed method provides an improvement in the image resolution, we present the results obtained with a 1D resolution test target. However, we want to profit this experimental section to show how the proposed approach works. The distance between the test and the grating to the CCD is 18 cm and 9 cm, respectively. Thus, the NA of the system is 0.0134 since we are considering the short width of the CCD. As diffraction grating we have used a Ronchi ruled grating having a period of 80 lp/mm. Figure 3 shows the Fourier transformation of the recorded hologram [Fig. 3(a)] when no reference beam is considered. Since we have 3 diffraction orders arriving at the CCD plane, the obtained spectrum is related with the autocorrelation terms corresponding with the Fourier transformation of the second, third and fourth lines in Eq. 10. Obviously, we are not in imaging conditions and the obtained spectral distribution will not have imaging capabilities. But when we insert the reference beam in a lensless Fourier holographic on-line configuration and capture a single hologram, the reference beam brings into focus the 3 band pass images [Fig. 3(b)]. However, real and virtual images (fifth and sixth lines in Eq. 10) overlap at the Fourier domain as a consequence of the on-axis configuration. Moreover, the in-focus images are also overlapping with the autocorrelation terms presented in Fig. 3(a). Therefore, it is impossible to recover separately the different band pass images.

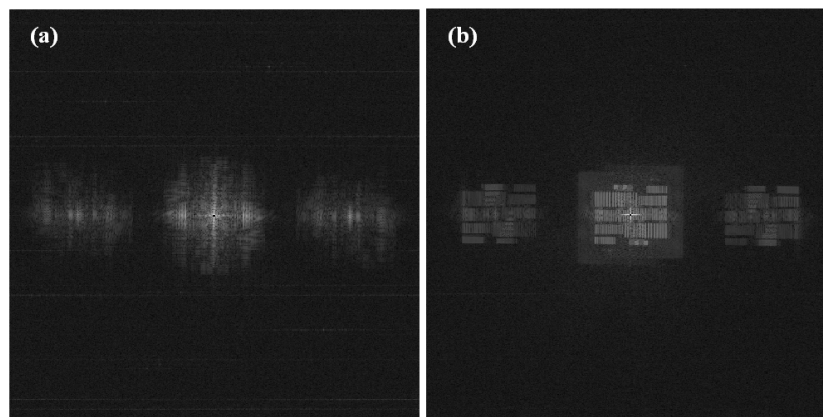


Fig. 3. (a) and (b) Fourier transformation of the recorded hologram without and with reference beam, respectively. The central spot has been blocked to enhance the contrast of the images.

To recover the complex amplitude distribution of the different band pass images at the Fourier domain, we can use off-axis holographic recording and Fourier filtering [Fig. 4(a)] and on-axis holographic recording and phase-shifting procedure [Fig. 4(b)]. However, the use of on-axis phase-shifting holography provides imaging capabilities in the whole frequency plane, as we can see in both images of Fig. 4. To obtain the image presented in Fig. 4(b), we apply the full phase-shifting cycle which is composed from 60 images. As a result, the virtual image, the autocorrelation terms and the zero order of the recorded hologram are eliminated and the different band pass images can be recovered by simple filtering in the Fourier domain.

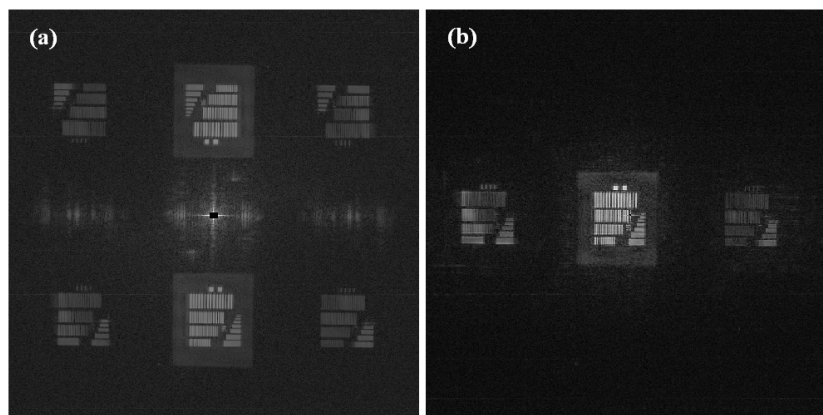


Fig. 4. Recovered band pass images when considering (a) off-axis holographic recording and (b) after applying the phase-shifting algorithm. The central spot has been blocked to enhance image contrast.

Finally, a superresolved image is obtained in terms of the generation of a synthetic aperture that expands up the cutoff frequency limit provided by the imaging system. The result is depicted in Figs. 5 and 6. In Fig. 5, the synthetic aperture and the superresolved image is depicted in comparison with the no grating case (conventional imaging mode). Without the grating, the resolution limit is defined by Element 4 of Group 2 (20 lp/mm or 50 μm). When performing the proposed approach, the resolution limit is reduced until Element 9 of Group 2 (60 lp/mm or 16.6 μm), which means a resolution gain factor of 3. For clarity reasons, Fig. 6 depicts the magnified area that is marked with a solid line white rectangle in Fig. 5(d) and plots a section of the last resolved element.

Aside the superresolution effect, we can notice how the vignetting of the conventional image is avoided in the superresolved one. Basically, the vignetting is originated because the aperture of the imaging system, that is, the CCD area, is not placed just at the Fourier plane because there is not a defined Fourier plane in the system. If we look at the borders of the object field of view, the image intensity becomes distorted and shadowed. However, this vignetting in the resulting image is avoided when the grating is inserted in the optical setup. If we pay attention to the left vertical bars of Elements 1 and 2 in the conventional image of the test [dashed white rectangle in Fig. 5(c)], we can see as they appear less defined than the others, that is, they appear a little bit blurred and with less intensity. However, the same vertical lines in the superresolved image appear perfectly defined. So aside a resolution image improvement, the final obtained image is free from vignetting problems.

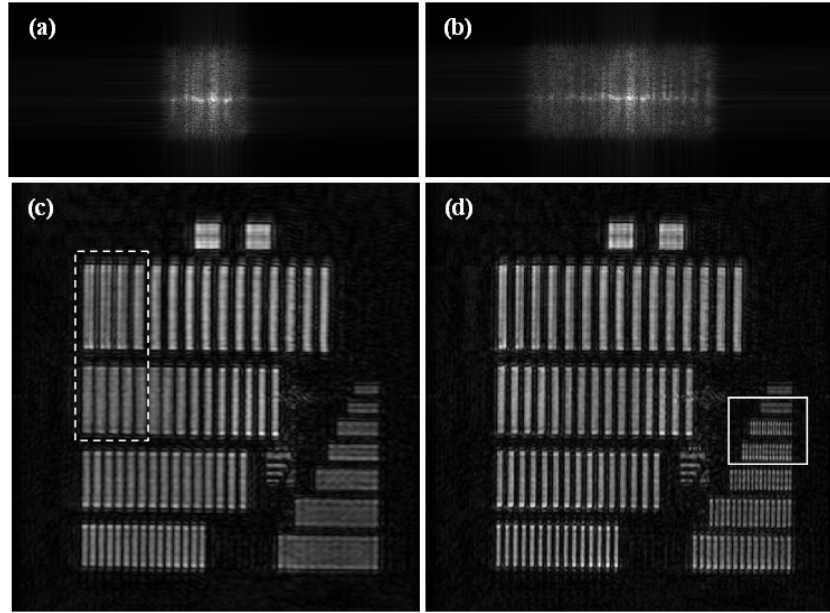


Fig. 5. (a) The conventional imaging system aperture, (b) the generated synthetic aperture, (c) the conventional image, and (d) the superresolved one.

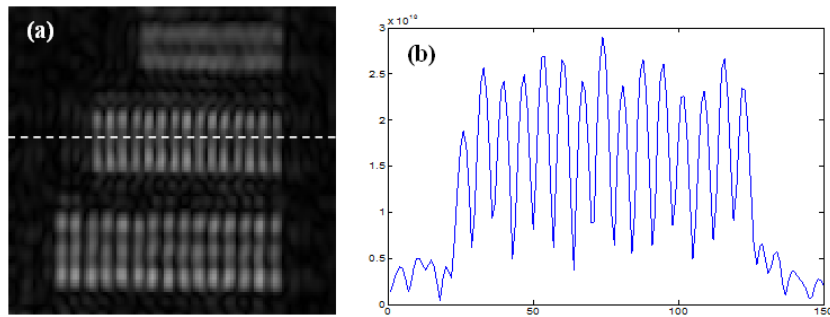


Fig. 6. (a) Magnified area marked with a white rectangle in Fig. 5(d), and (b) plot along the dashed white line of case (a).

3.2 Superresolution imaging for a 2D test object case

Once again, the distances between the USAF test and the grating to the CCD are the same than in the previous case. In order to achieve a 2D superresolution effect, we have used two Ronchi gratings placed in close contact but one at 90 degrees from the other. Both gratings have a period of 80 lp/mm. Figure 7 depicts two equivalent images to those ones presented in Fig. 3 but now due to the diffraction order combination of the two crossed gratings. In case (a) we can see the autocorrelation terms of the different band pass images when no reference beam is inserted and in case (b) we can see the focused band pass images when considering the reference beam superposed to the terms depicted in case (a).

Although the reference beam is not strictly introduced in on-line configuration (we can see as each pair of real and twin band pass images are a little bit shifted), we can see as the different band passes are overlapping [case (b)] and there is no possibility to recover them separately even if we consider off-axis holographic recording. So the only way to do that is by considering phase-shifting process. Figure 8(a) represents the recovery of the different band pass images. We can see as the whole frequency plane becomes optimized since the only

restriction to fulfill is the object field of view limitation needed in order that the band pass images will not overlap. In this case, the 3mm diameter of the laser beam is used as object field of view limitation without the need to add an external diaphragm (notice as the intensity of the recovered band pass images decreases from the center to the borders as it corresponds with a Gaussian laser beam profile). Cases (b) to (e) are the central part of the central, right, upper and oblique band pass images, respectively.

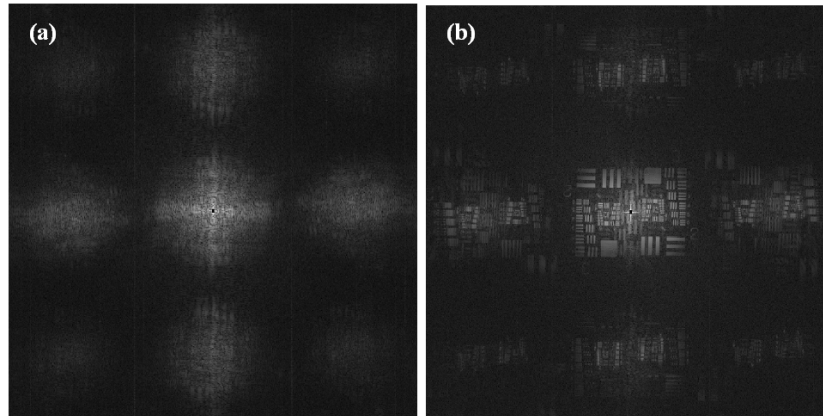


Fig. 7. Fourier transformation of the hologram recorded (a) without and (b) with reference beam. The central spot has been blocked to enhance image contrast.

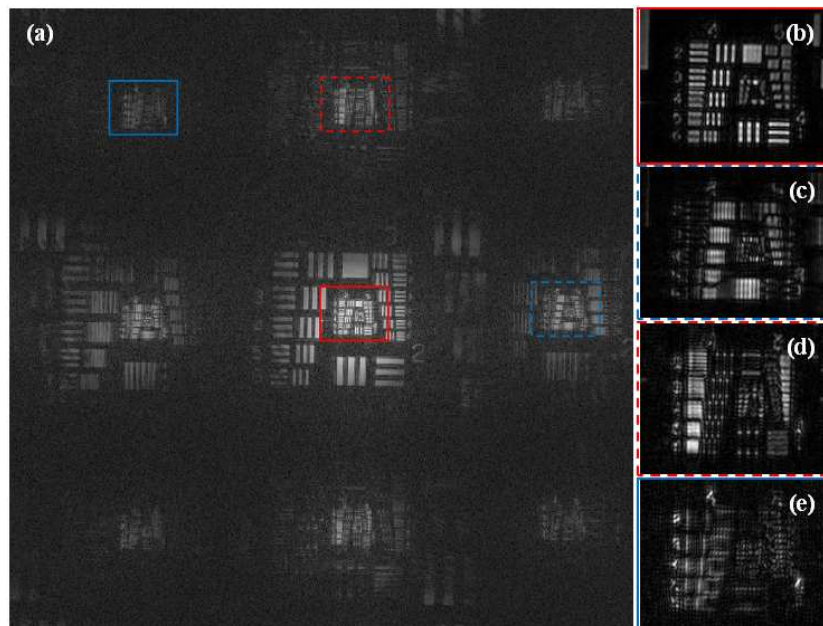


Fig. 8. (a) Whole Fourier domain image with the different band pass images resulting after applying the phase-shifting process and (b) to (e) are the magnified color rectangles of case (a) corresponding with the central region of the different band pass images.

Once the different band pass images are recovered by filtering process, they are used to assemble a synthetic aperture by replacing its spatial-frequency content by its original position in the object spectrum. And finally, a superresolved image is obtained by Fourier transformation of the information contained in the generated synthetic aperture. Figure 9

depicts the aperture of the imaging system in conventional imaging mode [case (a)], its corresponding conventional imaging [case (c)], the synthetic aperture generated as a consequence of the proposed approach [case (b)], and the superresolved image [case (d)].

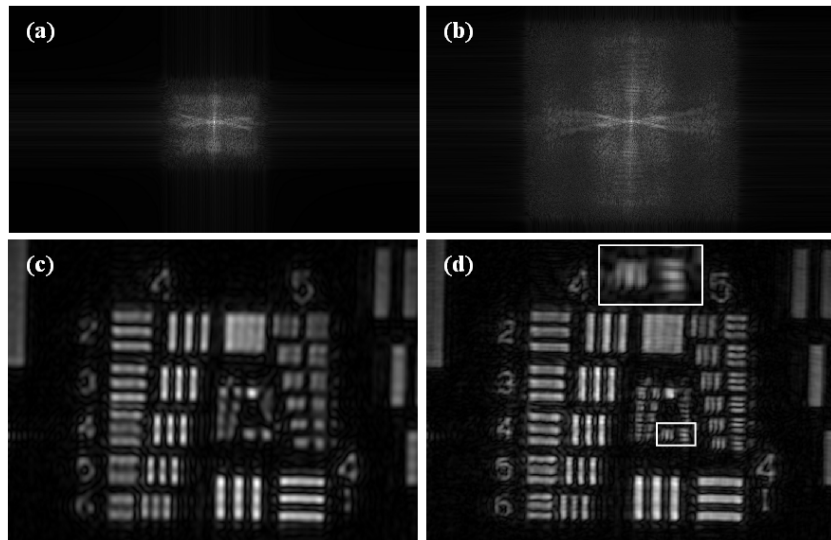


Fig. 9. (a)-(b) are the conventional imaging aperture and the generated synthetic aperture, respectively, and (c)-(d) are the conventional image and the superresolved one, respectively.

Since the CCD size is rectangular, the conventional imaging defines a different resolution in both main orthogonal directions. Thus, we find a resolution limit of $44\ \mu\text{m}$ (Group 4, Element 4) and $31.25\ \mu\text{m}$ (Group 5, Element 1) for the vertical (horizontal bars) and horizontal (vertical bars), respectively, as we can see in Fig. 9(c). As the position and basic frequency of the gratings are matched for the vertical direction, we should achieve a resolution improvement factor close to 3 in the horizontal bars and 1.4 times lower for the vertical ones. By taking a look at Fig. 9(d), we can see that the resolution limit is improved until $15.6\ \mu\text{m}$ (Group 6, Element 1) for both directions as the inset of Fig. 9(d) enhances. As predicted this new resolution limit means a resolution gain factor of 2.8 and 2 for vertical and horizontal directions, respectively.

4. Conclusions

We have presented a step forward in superresolved digital imaging considering a lensless Fourier holographic configuration. It is based on the insertion of diffraction gratings in the optical assembly in such a way that high order diffracted components are redirected towards the imaging device. The way to recover this additional information inaccessible without using the gratings is by applying on-axis holographic recording and phase-shifting method. This procedure allows the usage of the whole frequency plane as imaging plane and produces an optimization in the information capacity that the imaging system has in comparison with the off-axis holographic recording used in other similar approaches [28-30]. This fact means that, for a given object field of view, we can improve the gain in resolution by considering a grating having a high number of diffraction orders that will allow a high number of recovered band pass images, or, for a given resolution gain factor, we can get superresolved imaging over a large field of view. Moreover, derived from the fact of inserting a grating in the setup, the final reconstructed image will exhibit reduced vignetting problems.

Additional improvements come from an experimental point of view. Unlike in other similar approaches where it is theoretically possible to achieve high resolution gain factors but

more modest ones were experimentally validated [28,30], we have experimentally demonstrated a resolution gain factor of 3. Moreover, those previous attempts were only validated for 1D objects, although Ref. [30] exhibits theoretical 2D capabilities. Now, we have presented experimental results for a 2D object. And finally, the work reported in Ref. [30] considered three different directions in the 2D frequency space that are coming from the hexagonal grating that was used. Now we have proposed a 2D implementation with four different directions, which is a more natural expansion of the rectangular aperture of the imaging system.

Acknowledgements

This work was supported by the Spanish Ministerio de Educación y Ciencia and FEDER funds under the project FIS2007-60626. Luis Granero wants to thank AIDO for the time dedicated to this research.